Contents lists available at ScienceDirect

Thermal Science and Engineering Progress

A novel CFD model for design and performance prediction of recuperators for Indirect Evaporative Cooling

Roberta Caruana [*], Luca Marocco, Manfredo Guilizzoni

Department of Energy, Politecnico di Milano, Via Lambruschini 4, 20156 Milan, Italy

ABSTRACT

Indirect evaporative cooling (IEC) appears to be a highly promising technology for incorporating and/or substituting traditional air conditioning systems, as it can guarantee good cooling performance with a reduced environmental impact. In this study, a Computational Fluid Dynamics (CFD) model for design and performance prediction of recuperators for IEC systems with dry primary and secondary channels was developed. The model was validated against experimental data for a cross-flow recuperator, obtaining a maximum difference between numerical and experimental results of 4.9% for the secondary air outlet temperature, 5.3% for the primary air outlet temperature, and 8.1% for the dry-bulb effectiveness. After validation, the model was used to find a new plate geometry which guarantees a 12.5-15.9% improvement in the dry-bulb effectiveness, without an excessive increase in the pressure losses along the channels.

1. Introduction and state of the art

At present, heating, ventilation, and cooling systems are responsible for half of the total energy consumption in buildings [1]. In particular, cooling of indoor environments has become increasingly energy demanding, both for the greater request of adequate thermohygrometric conditions, and for the rising of outdoor temperatures due to climate change [2–4]. For this reason, the necessity of new effective cooling technologies, able to minimize the energy use, arose [5,6].

Indirect evaporative cooling (IEC), which consists in using the latent heat of evaporation of water to remove thermal power from another fluid, seems a very promising technology to integrate and/or replace traditional air conditioning systems, particularly in hot and dry regions [7]. An air-to-air IEC system is usually composed of alternating primary and secondary channels, separated by thin conductive plates. Product (or primary) air flows inside the primary channels, while working (or secondary) air flows inside the secondary channels [8,9]. Water is delivered by a pump and it is either directly introduced into the secondary channels, with the aim of generating a film on the heat exchanger plates [10], or it is used to pre-humidify the secondary air before it enters the recuperator, in order to avoid direct contact with the plates, which can cause problems of corrosion and aging. In this second case, the evaporative process takes place upstream of the heat exchanger, and when the secondary air enters the secondary channels of the recuperators, it is already cooled and humidified. Therefore, in this case, no liquid water is introduced into the secondary channels, which remain dry.

As IEC systems are able to reduce the air temperature without increasing its humidity ratio, they can be used for many applications which require these characteristics, as residential buildings [11], greenhouses [12], and pharmaceutics [13]. Consequently, the development of models able to predict the behavior and performance of IEC systems has become a necessity, particularly in recent years [14]. In fact, using a model for the early design of IEC systems allows to reduce the need for potentially complex and expensive experimental campaigns.

The models currently available in literature can be divided into two macro-categories: analytical and numerical.

For what concerns analytical models, the first approaches to the IEC technology were made in 1998 by Alonso et al. [15], who developed a model based on the definition of an equivalent temperature, thus studying the primary and secondary air flows separately, and by Stoitchkov and Dimitrov [16], who estimated the mean surface water temperature, and took into account the barometric pressure. Then, Ren and Yang [17] introduced the possibility of having non-unitary Lewis number and surface wettability factor, and took into account also the effects of spray water evaporation, temperature variations, and enthalpy changes. Hasan [18] developed a model based on the ε-NTU method, assuming a linear saturation temperature-enthalpy relation, and redefining the potential gradients, heat capacity rate parameters, and transfer coefficient. Liu et al. [19] proposed another model based on modifying the ε-NTU method through the iterative estimation of the enthalpy change/temperature change ratio in the wet channels. Cui

---

* Corresponding author.
E-mail address: roberta.caruana@polimi.it (R. Caruana).

Nomenclature

Latin letters

$\dot{M}$	Mass flow rate (kg/s)
$\dot{Q}''$	Heat flux (W/m^2)
$\dot{V}$	Volumetric flow rate (m^3/h)
$\mathbf{U}$	Velocity vector (m/s)
c_p	Specific heat capacity at constant pressure (J/(kg K))
F_1	Turbulence model coefficient (−)
h	Specific enthalpy (J/kg)
K	Specific kinetic energy (J/kg)
k	Specific turbulent kinetic energy (J/kg)
p	Pressure (Pa)
P_k	Turbulent kinetic energy production term (Pa/s)
p_{rgh}	Hydrostatic pressure (Pa)
R^*	Specific gas constant (J/(kg K))
Re	Reynolds number (−)
T	Temperature (K)
t	Time (s)
y^+	Dimensionless wall distance (−)

Greek letters

α	Thermal diffusivity (m^2/s^2)
β	Turbulence model coefficient (−)
β^*	Turbulence model coefficient (−)
γ	Turbulence model coefficient (−)
μ	Dynamic viscosity (Pa s)
ν	Kinematic viscosity (m^2/s^2)
ω	Specific turbulent dissipation rate (1/s)
ρ	Density (kg/m^3)
σ_ω	Turbulence model coefficient (−)
σ_k	Turbulence model coefficient (−)
$\sigma_{\omega2}$	Turbulence model coefficient (−)

Subscripts

eff	Effective
in	Inlet
int	Interface
out	Outlet
P	Primary air
S	Secondary air
t	Turbulent

Abbreviations and acronyms

AHU	Air Handling Unit
CFD	Computational Fluid Dynamics
DIEC	Dew-point Indirect Evaporative Cooling
IEC	Indirect Evaporative Cooling
SST	Shear Stress Transport

considering the adiabatic cooling of the working air in the inlet plenum and the wettability of the plates. Comino et al. [24] considered the effects of variable water flow rate. Finally, Zheng et al. [25] took into account the thermal resistance of the condensate film.

Numerical models for IEC systems have gained popularity in recent years, as they can guarantee a greater accuracy than analytical models, which are often based on many simplifying assumptions [14]. Zhao et al. [26] developed a numerical model for evaluating the suitability of dew-point indirect evaporative cooling (DIEC) systems in hot and dry regions. Riangvilaikul and Kumar [27] used a numerical model to evaluate the influence of the inlet air temperature and humidity on the dew-point effectiveness of a DIEC system. Cui et al. [28] evaluated the influence of the design parameters on the performance of a new type of DIEC system through a computational fluid dynamics (CFD) model. Wan et al. [29] presented a 2-D CFD model for improving the accuracy of the 1-D analytical model of Ren and Yang [17]. Wan et al. [30–32] developed a CFD model for evaluating the heat and mass transfer coefficients, and the Nusselt and Sherwood numbers in DIEC systems. You et al. [33] used a CFD model to evaluate the influence of some design parameters on the performance of cross-flow IEC systems. Min et al. [34] presented a numerical model for comparing the performance of a counter-flow and a cross-flow IEC systems, also optimizing the geometrical parameters. Pakari and Ghani [35,36] developed a 1-D and a 3-D CFD regression models, for the performance prediction, design, and optimization of DIEC systems. Liu et al. [37] presented a model that introduced the coupling of the heat and mass transfer equations with the energy equation. Guo et al. [38] developed a numerical model for evaluating the effect of the condensation area ratio on the IEC system performance. Wan et al. [39] used a CFD model to conduct a single-factor and a multiple-factor analysis on the design parameters to improve the correlations for the mean heat and mass transfer co-efficients. Adam et al. [40] used a numerical model to evaluate the effects of the wettability factor on the IEC system performance. Shi et al. [41] developed a CFD model, considering the non-uniformity in temperature and humidity along the channel width. Comino et al. [42] used a modified ϵ-NTU numerical model for the optimization of a DIEC system. Adam et al. [43] used a numerical model to evaluate the effects of different condensation states in a cross-flow IEC system. Zhu et al. [44] evaluated the effects of a non-uniform water distribution along the DIEC system plates through a CFD model. Pacak et al. [45] developed a CFD model to evaluate the pressure loss along the dry channels of a counter-flow IEC system. Adam et al. [46] presented a CFD model for the analysis of the influence of the plates shape on the performance of counter-flow IEC systems. Finally, Ma et al. [47] developed a CFD model considering the water spray configuration and water film distribution in the performance analysis.

A more accurate and in-depth analysis of the previously mentioned models can be found in the review by Caruana et al. [14].

All the models available in literature refer to IEC systems in which the secondary air flowing into the recuperator channels is in direct contact with water. However, as previously mentioned, in some applications the working air is humidified before entering the heat exchanger channels, and the excess water is removed. Therefore, the recuperators of these IEC systems work in dry conditions.

The scope of this work is to develop a simple and accurate CFD model for design and performance prediction of recuperators for IEC applications with dry primary and secondary channels. The model was implemented in OpenFOAM, and it was validated against experimental results obtained for a cross-flow recuperator. After being validated, the model was used to find a new plates geometry which guarantees a performance enhancement avoiding an excessive increase in the pressure loss along the channel, and thus in the energy consumption.
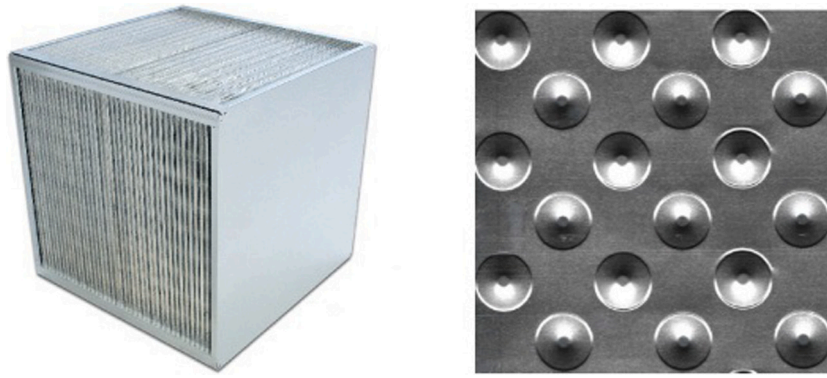
et al. [20] developed a model based on the logarithmic mean temperature difference method, introducing the enthalpy/wet bulb temperature ratio, a modified overall heat transfer coefficient, and a driving-force based on the wet-bulb temperature. Chen et al. [21] proposed a model which considers also the possibility of condensation in the dry channels. De Antonellis et al. [22,23] developed a phenomenological model

Fig. 1. Analyzed IEC heat exchanger (left) and clip of a dimpled plate (right).

2. Experimental tests

In order to validate the model described in this work, several experimental tests concerning an air-to-air cross-flow recuperator were used. The air inlet temperatures and flow rates chosen for the tests were used as input data for the model, while the air outlet temperatures were used for comparison with the numerical results.

2.1. Analyzed IEC heat exchanger

The recuperator analyzed in this work is a commercial air-to-air IEC heat exchanger in cross-flow configuration (Fig. 1). The system is composed of 119 aluminum squared plates (gross side length: 500 mm, net side length at the extremities: 440 mm), which form 59 channels that constitutes the airflow passages, alternating a primary and a secondary air channel. The plates are clamped at the extremities to the adjacent ones, in order to avoid mixing of the primary and secondary air flows. Furthermore, neighboring plates are in contact with each other over the entire surface by protruding dimples, which guarantee mechanical stiffness. Therefore, a pattern of concave and convex dimples in the shape of spherical caps can be observed on each plate (Fig. 1). The dimples are slightly flattened at the top, in order to improve mechanical stability when in contact with the ones of the adjacent plates. The base diameter of the dimples is 20 mm, their height is 1.615 mm, and the spacing between the extremities of two concave or convex dimples is 30 mm.

2.2. Experimental apparatus

The experimental apparatus used for the validation tests, which has been originally designed to evaluate the performance of rotative heat exchangers, plate heat exchangers, and desiccant wheels [48,49], is able to guarantee the desired supply air conditions during the experimental tests. In particular, two air handling units (AHUs) process the primary and secondary air streams separately, while various heating coils, cooling coils, and adiabatic humidifiers control the supply air temperature and humidity. Moreover, an additional electric heater is placed in the AHU of the secondary air flow, in order to increase its temperature up to 100 °C [50]. The air flow rates are controlled through variable speed fans, which can guarantee a maximum volumetric flow rate of 1400 m³ h⁻¹ for the primary air, and of 2000 m³ h⁻¹ for the secondary air [22]. Inlet and outlet air temperatures are measured through RTD PT100 probes, placed upstream and downstream of the heat exchanger, which show a ±0.2 °C uncertainty.

A more in-depth description of the experimental setup can be found in previous works [48,49].

Table 1
Summary of the inlet volume flow rates, temperatures, and Reynolds numbers for the analyzed cases.

	Case code	$\dot{V}_{Sin}$ [m³ h⁻¹]	$\dot{V}_{Pin}$ [m³ h⁻¹]	T_{Sin} [K]	T_{Pin} [K]	Re_{Sin} [–]	Re_{Pin} [–]
Unbalanced	A	1012	745	303.25	323.35	672	495
	B	1077	683	303.45	324.45	715	453
	C	1006	831	304.35	334.75	664	548
	D	1008	848	305.15	339.75	662	557
	E	1294	909	305.55	328.25	848	596
Balanced	F	1260	1240	303.75	308.45	835	821
	G	1259	1241	303.55	308.35	835	823
	H	1247	1278	303.15	308.25	829	849
	I	1059	1086	302.97	315.77	705	723
	J	1263	1315	303.33	315.70	839	873

2.3. Adopted methodology

In this study, 10 experimental tests with different air flow rates and temperatures have been used in order to validate the model. A summary of the inlet flow rates, temperatures, and Reynolds numbers for the analyzed cases can be found in Table 1, where $\dot{V}$ is the volumetric flow rate, T is the temperature, Re is the Reynolds number, the subscript P refers to the primary air, the subscript S refers to the secondary air, and the subscript in refers to inlet conditions.

It is worth noticing that in the cases A–E the primary and secondary air volume flow rates are significantly different, while in the cases F–J the ratio between the secondary and primary air flow rates is always in the range 0.96–1.02, so the two flow rates can be considered practically equal. Consequently, cases A–E will be denoted as those with "unbalanced" flow rate, and cases F–J will be those with "balanced" flow rates.

For achieving the model validation, the experimental values of the outlet air temperatures and dry-bulb effectiveness have been compared to the numerical results. As previously mentioned, the temperatures were measured through RTD probes, while the dry bulb effectiveness, ε_{DB}, was computed as the ratio between the thermal power exchanged and the maximum thermal power exchangeable in those flow and temperature conditions, that is:

$$\varepsilon_{DB} = \frac{\left(\dot{M}c_p\right)_P \cdot \left(T_{Pin} - T_{Pout}\right)}{\left(\dot{M}c_p\right)_{min(P,S)} \cdot \left(T_{Pin} - T_{Sin}\right)} \tag{1}$$

where: $\dot{M}$ is the mass flow rate, c_p is the specific heat capacity at constant pressure, and the subscript out refers to outlet conditions.

The experimental uncertainties were computed as in previous works of the same research group [22,50], in accordance with the reference international standard [51].
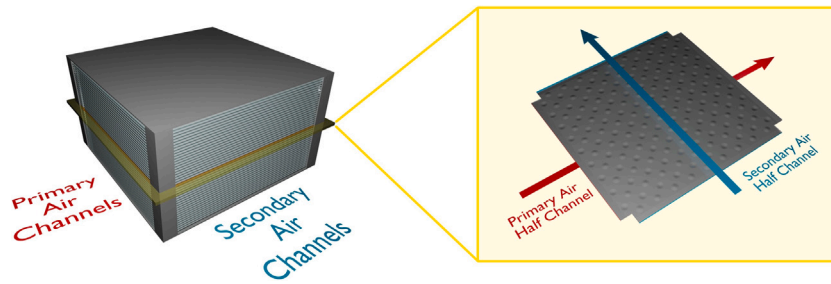
Fig. 2. Scheme of the real domain (left) in relation with the simulated domain (right).

3. Numerical model

The numerical model described in this work was developed through the open-source software OpenFOAM v9, which is written in C++ and it is based on the finite volume method.

The model is based on the following assumptions: (a) the secondary air is humidified before entering the recuperator, and excess water is removed, so that both the primary and secondary channels work in dry conditions; (b) air is modeled as an ideal gas, with constant dynamic viscosity, thermal conductivity, and specific heat capacity; (c) the heat exchanger external walls are perfectly insulated, so they can be considered adiabatic; (d) the effects of gravity are negligible; (e) the air inlet velocities are uniform; (f) the possibility of condensation of the vapor in the primary air is neglected; (g) all radiative heat exchanges are neglected.

3.1. Simulated domain

As previously mentioned, the heat exchanger simulated in this work is composed of 59 channels and 119 plates. However, the geometry and structure of these channels are the same in the whole recuperator. Therefore, it is not necessary to simulate the entire heat exchanger, as symmetries can be exploited.

For this reason, the computational domain is composed of two half-channels, one for primary and one for secondary air, separated by a thin baffle representing a dimpled plate. A scheme of the simulated domain in relation with the real domain is shown in Fig. 2, and the domain boundaries are shown in Fig. 3.

3.2. Solver and governing equations

As the computational domain is composed of two fluid regions (primary and secondary air), the *chtMultiRegionFoam* solver was used for the numerical calculations. The solution strategy followed by this solver is segregated, namely the equations for each variable characterizing the system are solved sequentially. Moreover, both steady and transient flows with or without turbulence modeling are allowed.

The governing equations that are solved for each fluid during every iteration are the mass, momentum, and energy conservation, written as:

$$\frac{\partial \rho}{\partial t} + \nabla \cdot (\rho \mathbf{U}) = 0 \tag{2}$$

$$\frac{\partial (\rho \mathbf{U})}{\partial t} + \nabla \cdot (\rho \mathbf{U} \otimes \mathbf{U}) = -\nabla p_{rgh} + \nabla \cdot \left(\mu_{eff} \nabla \mathbf{U} \right) \tag{3}$$

$$\frac{\partial (\rho h)}{\partial t} + \frac{\partial (\rho K)}{\partial t} + \nabla \cdot (\rho K \mathbf{U}) - \frac{\partial p}{\partial t} = \nabla \cdot \left(\rho \alpha_{eff} \nabla h \right) \tag{4}$$

where: ρ is the fluid density; t is the time; $\mathbf{U}$ is the velocity vector; p_{rgh} is the hydrostatic pressure; μ_{eff} is the effective dynamic viscosity, which includes the dynamic viscosity and the turbulence contribution, if present; h is the specific enthalpy; $K = \frac{|\mathbf{U}|^2}{2}$ is the specific kinetic energy; p is the pressure; and α_{eff} is the effective thermal diffusivity,

which includes the thermal diffusivity and the turbulence contribution, if present.

As air is treated as an ideal gas in the model, the equation of state for ideal gases must be included as:

$$p = \rho R^* T \tag{5}$$

where R^* is the specific gas constant.

If turbulence modeling is included, the equations for the turbulent variables should be added. If the $k - \omega$ shear stress transport (SST) model is selected, as in the present work, the two equations for the specific turbulent kinetic energy and the specific turbulent dissipation rate can be written as:

$$\frac{\partial (\rho k)}{\partial t} + \nabla \cdot (\rho \mathbf{U} k) = P_k - \beta^* \rho \omega k + \nabla \cdot \left[\left(\mu + \sigma_k \mu_t \right) \nabla k \right] \tag{6}$$

$$\frac{\partial (\rho \omega)}{\partial t} + \nabla \cdot (\rho \mathbf{U} \omega) = \frac{\gamma \rho}{\mu_t} P_k - \beta \rho \omega^2 + \nabla \cdot \left[\left(\mu + \sigma_\omega \mu_t \right) \nabla \omega \right] + 2 \left(1 - F_1 \right)$$
$$\times \frac{\rho \sigma_{\omega 2}}{\omega} \nabla k \cdot \nabla \omega \tag{7}$$

where: k is the specific turbulent kinetic energy; ω is the specific turbulent dissipation rate; μ is the dynamic viscosity; μ_t is the turbulent eddy viscosity; P_k represents the turbulent kinetic energy production term; σ_k, σ_ω, $\sigma_{\omega 2}$, β^*, β, γ, and F_1 are model coefficients, which are thoroughly described in [52].

Finally, the two fluid regions are coupled by a boundary condition which imposes that the absolute value of the heat flux leaving a fluid region at the interface must be equal to the absolute value of the heat flux entering the other fluid region at the same interface, namely:

$$\dot{Q}''_{P,int} = -\dot{Q}''_{S,int} \tag{8}$$

where $\dot{Q}''_{P,int}$ and $\dot{Q}''_{S,int}$ are the two heat fluxes at the interface between the two regions, that are assumed to be positive when entering a region, negative when leaving it.

3.3. Initial conditions and boundary conditions

The boundary conditions used for velocity, U, temperature, T, pressure, p, and hydrostatic pressure, p_{rgh}, are summarized in Table 2. The initial conditions selected for each of these variables were extracted from the experiments.

The boundary conditions used for the turbulent variables, namely turbulent thermal diffusivity, α_t, specific turbulent kinetic energy, k, turbulent kinematic viscosity, ν_t, and specific turbulent dissipation rate, ω, can be found in Table 3. The initial conditions for these variables were estimated through the usual formulas for the mixing length and turbulent intensity, assuming a turbulent Prandtl number equal to 0.85.

3.4. Simulations settings

For more than half of the validation cases, both stationary simulations with first order discretization schemes and transient simulations with second order discretization schemes were carried out, as the first ones require a lower computational time and the second ones are more

Table 2
Summary of the boundary conditions for velocity, temperature, pressure, and hydrostatic pressure used in OpenFOAM.

Boundaries	U	T	p	p_{rgh}
Inlets	fixedValue	fixedValue	calculated	zeroGradient
Outlets	pressureInletOutletVelocity	zeroGradient	calculated	fixedValue
Dimpled plate	fixedValue	compressible::turbulentTemperatureCoupledBaffleMixed	calculated	fixedFluxPressure
External sides	fixedValue	zeroGradient	calculated	fixedFluxPressure
Top and bottom	symmetryPlane	symmetryPlane	symmetryPlane	symmetryPlane

Table 3
Summary of the boundary conditions for the turbulent variables used in OpenFOAM.

Boundaries	α_t	k	ν_t	ω
Inlets	calculated	turbulentIntensityKineticEnergyInlet	calculated	turbulentMixingLengthFrequencyInlet
Outlets	calculated	zeroGradient	calculated	zeroGradient
Dimpled plate	compressible::alphatWallFunction	kqRWallFunction	nutkWallFunction	omegaWallFunction
External sides	compressible::alphatWallFunction	kqRWallFunction	nutkWallFunction	omegaWallFunction
Top and bottom	symmetryPlane	symmetryPlane	symmetryPlane	symmetryPlane

accurate. In particular, in the stationary cases the simulations were stopped after reaching a steady condition, with stable average values of the physical quantities, namely after a number of iterations between 15 000 and 25 000, while in the transient cases the simulations were stopped after reaching a statistically-steady condition, namely in a time between 1 and 4 s. The maximum time step for the transient simulations was set to 10^{-4} s, but the effective time step was automatically selected by the software, in order to maintain a Courant number below 0.5.

For stationary simulations, the thermophysical properties values selected as final results were chosen by taking the weighted average of the considered property over a certain boundary at the final iteration. On the contrary, for the transient simulations, the final values were calculated by averaging over all time steps, after reaching a statistically-stationary condition, the weighted averages of the considered property over a certain boundary.

3.5. Mesh and mesh independence

The mesh was built using the *blockMesh* and *snappyHexMesh* utilities available in OpenFOAM. In particular, *blockMesh* was used to develop a background orthogonal mesh and to define the boundaries of the domain representing planes of symmetry. After that, *snappyHexMesh* was used to define the other boundaries of the domain (inlets, outlets, and walls), to separate the two fluid regions for primary and secondary air, and to trim and adapt the background mesh, in order to obtain the desired mesh characteristics.

A schematic diagram representing the mesh and its boundaries is shown in Fig. 3.

The mesh independence was assessed for two preliminary cases, differing in inlet air temperatures and velocities. In particular, seven meshes with a number of cells varying from 676k and more than 18M were tested, and these analyses showed that the difference in the primary air outlet temperatures among all the cases was within 1.5%. Therefore, a mesh composed of about 4.9M cells was selected, as a suitable compromise between computational cost and mesh characteristics which allow to capture the fluid behavior in the boundary layer.

The quality of the mesh, composed only of hexahedral cells, resulted in a maximum aspect ratio around 17, a maximum skewness of about 3.1, an average and maximum non-orthogonality around 7.55° and 66.9°, respectively, and an average value of dimensionless wall distance, y^+, below 1. Therefore, the quality of the final mesh is considered acceptable, also taking into account that one of the main aims of this work is to develop a model that can be used in normal design conditions, without requiring too many computational resources. In fact, a finer mesh may have allowed to better capture the boundary layer in contact with the dimpled plate, but it would have further increased the already quite high simulation times.

These considerations about the mesh also reinforce the choice of performing simulations using a turbulence model. In fact, the flow

Table 4
Summary of the simulations settings for the test cases.

Setting code	Turbulence	Discretization order	Transient
Numerical 1	No	1st	No
Numerical 2	Yes	1st	No
Numerical 3	No	2nd	Yes
Numerical 4	Yes	2nd	Yes

conditions may be seen as "borderline" between laminar and turbulent, as the Reynolds number in the dimpled channels is lower than 1000, thus a dominantly laminar behavior would be expected, but the dimples may act as cross-flow obstacles and, combined to intrinsically time-varying phenomena, may favor an early onset of turbulence, at least in some regions. Consequently, some of the simulations were performed using both laminar and turbulent settings, in order to compare the results and select the most accurate solution.

4. Validation

As previously mentioned, the validation of the model was performed by comparing the numerical and experimental results in terms of outlet air temperatures and dry-bulb effectiveness. In particular, three test cases with unbalanced flow rates (A, B, C), and three test cases with balanced flow rates (F, H, J) were selected, and they were tested with four different settings, in order to choose the simulation condition able to better predict the experimental results. The four types of settings used for simulating the test cases are summarized in Table 4.

The numerical and experimental secondary air outlet temperatures, T_{Sout}, primary air outlet temperatures, T_{Pout}, dry-bulb effectivenesses, ε_{DB}, and the experimental uncertainties for all the test cases are shown in Figs. 4, 5, and 6, respectively.

From these figures, it is possible to notice that the simulations settings which lead to a better prediction of the experimental results are always the ones denoted with "Numerical 4" (blue circles in the figures), namely with turbulence, second order discretization schemes, and transient conditions. In particular, using these settings, the maximum error is about 4.9% for the secondary air outlet temperature, 5.3% for the primary air outlet temperature, and 8.1% for the dry-bulb effectiveness. Therefore, the "Numerical 4" settings were selected for all the following simulations.

It is worth mentioning that using the simulations settings denoted with "Numerical 2" (green circles in the figures), namely with turbulence, first order discretization schemes, and stationary conditions, the maximum error is about 7.0% for the secondary air outlet temperature, 7.5% for the primary air outlet temperature, and 12% for the dry-bulb effectiveness, but the required computational time for each simulation is about a sixth of the one necessary when using "Numerical 4" settings. In fact, using 16 Intel Xeon Gold 6248 processors, the required
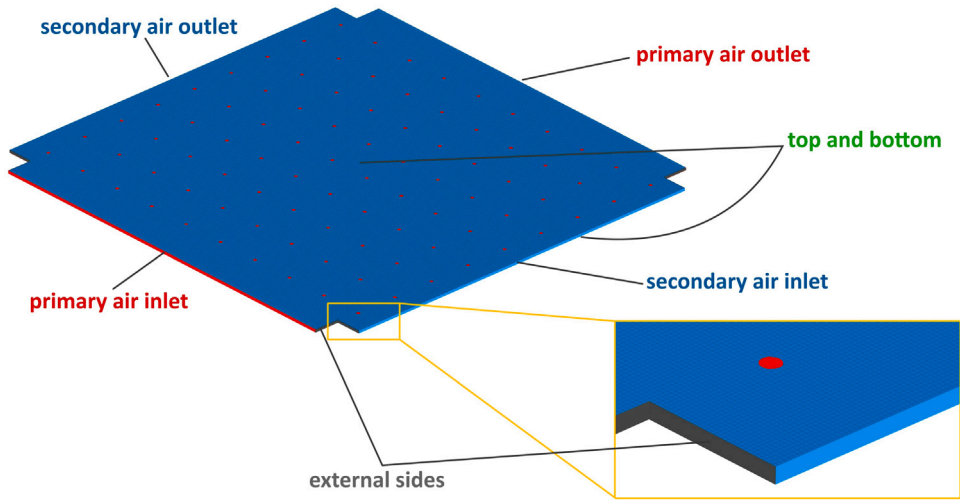
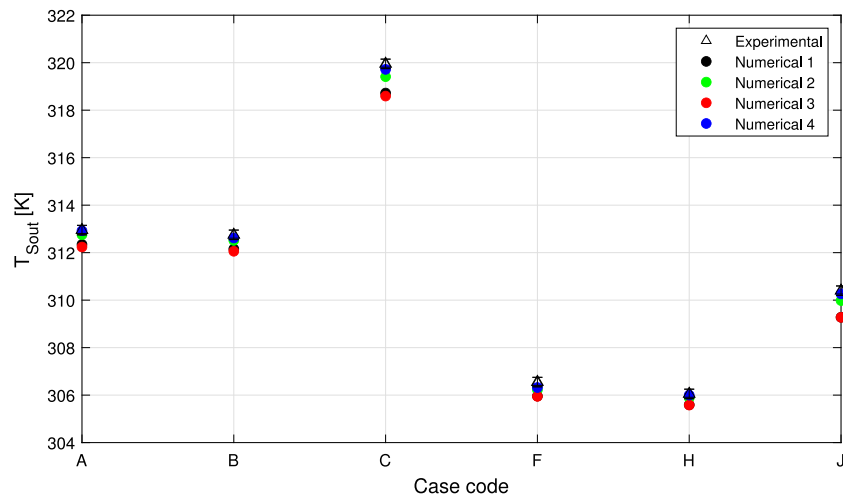**Fig. 3.** Scheme of the mesh and its boundaries.

Fig. 4. Secondary air outlet temperatures for the test cases.
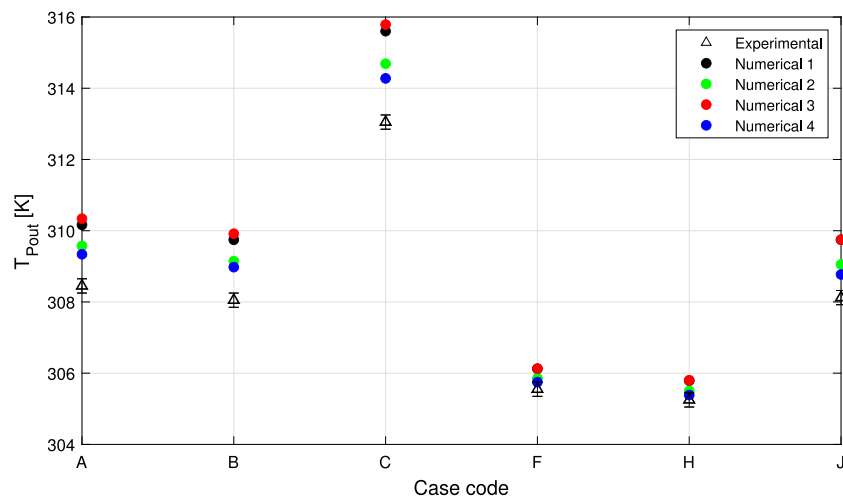

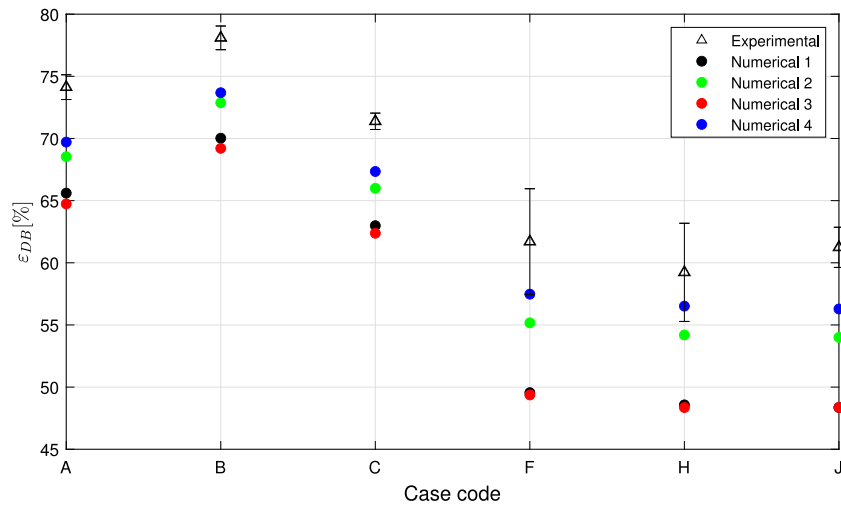**Fig. 5.** Primary air outlet temperatures for the test cases.

Fig. 6. Dry-bulb effectiveness for the test cases.
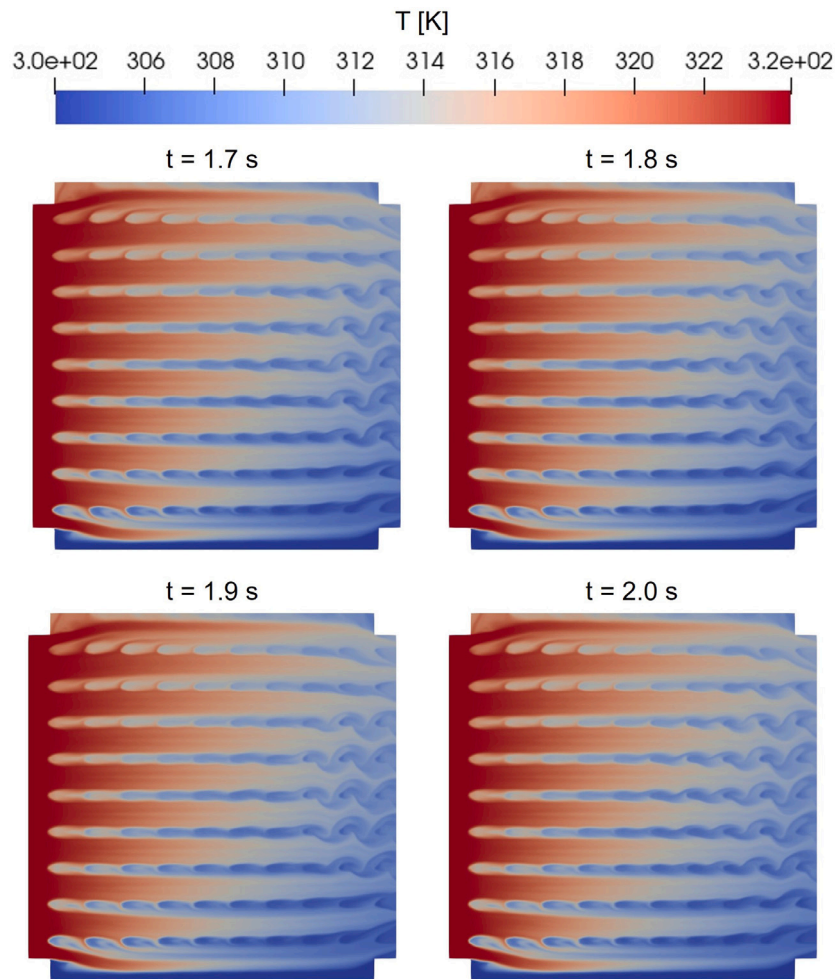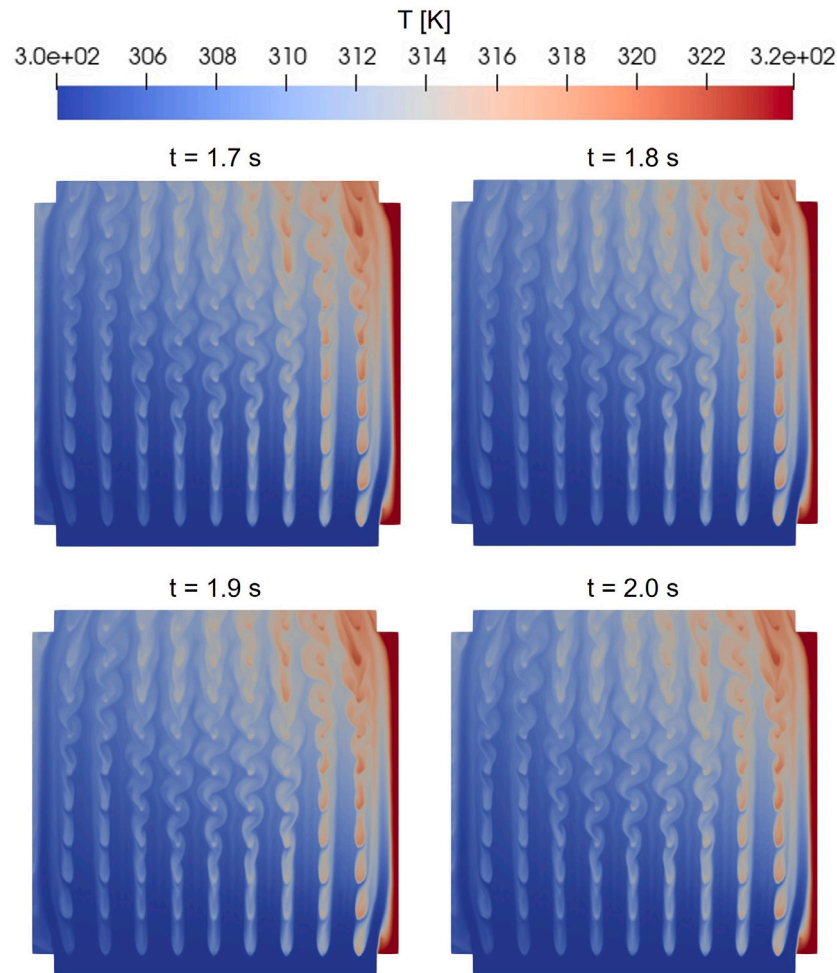

Fig. 7. Primary air temperature for time steps 1.7, 1.8, 1.9, and 2.0 s in the simulation of case B, obtained with the "Numerical 4" settings.

computational time is in the range 20–22 h with the "Numerical 2" settings, while it is about 120–130 h when using the "Numerical 4"

settings. Consequently, the "Numerical 2" settings can be considered a good trade-off between accuracy and computational cost.

Fig. 8. Secondary air temperature for time steps 1.7, 1.8, 1.9, and 2.0 s in the simulation of case B, obtained with the "Numerical 4" settings.

The results confirmed that adding the turbulence equations to the model led to better results than those obtained in laminar conditions. Moreover, the simulations with second order discretization schemes in transient conditions were closer to the experimental results than those with first order discretization schemes in steady conditions. In fact, as usual, second order schemes are more precise than first order ones, but the flow is also intrinsically transient, as it presents von-Kármán vortex streets, shown in Figs. 7 and 8.

These figures show the primary and secondary air temperature fields obtained in the simulation of case B, for four time steps in a statistically-steady condition. In particular, it is possible to notice that, as expected, the von-Kármán vortex streets are more evident for secondary air than for primary air, as in this case the secondary air inlet flow rate is significantly higher than that of the primary air.

As the "Numerical 4" settings led to the best prediction of the experimental results, two more validation cases with unbalanced flow rates, namely D and E, and two with balanced flow rates, namely G and I, were simulated with these settings.

The results of all the validation cases simulated with the "Numerical 4" settings, compared with the corresponding experimental results can be seen in Figs. 9, 10, and 11, which show the secondary air outlet temperatures, primary air outlet temperatures, and dry bulb effectivenesses, respectively.

Taking into account all the test cases, the average errors are about 1.7% for the secondary air outlet temperature, 4.0% for the primary

air outlet temperature, and 6.0% for the dry-bulb effectiveness. Consequently, the difference between the numerical and experimental results obtained with these settings can be considered acceptable to ensure model validation.

5. Results and discussion

After validation, the possibility of changing the plate shape to improve the cooling performance was investigated. For this analysis, the inlet conditions of a case with unbalanced flow rate (case C), and a case with balanced flow rates (case I) were used.

Firstly, simulations using a flat plate channel without dimples were carried out, in order to establish a reference. The results of this analysis showed that the previously described dimples have a very minor effect on the heat exchange. In fact, the comparison between the results obtained with the dimpled plate and the flat plate shows a maximum difference of 2% in terms of dry-bulb effectiveness. This result is due to the fact that the ratio between dimples maximum diameter and height is very high. Consequently, the dimples, which are necessary for mechanical requirements, have a very minor effect on the heat exchanger effectiveness, as they are too flat and smooth to significantly alter the fluid flow.

For this reason, other types of dimples which could potentially improve the heat exchange while satisfying the mechanical requirements of structural stability and stiffness were investigated. In particular,
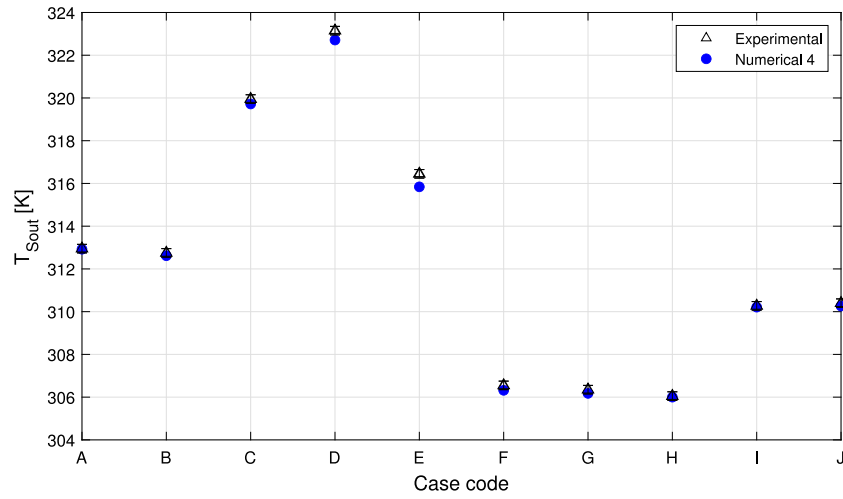
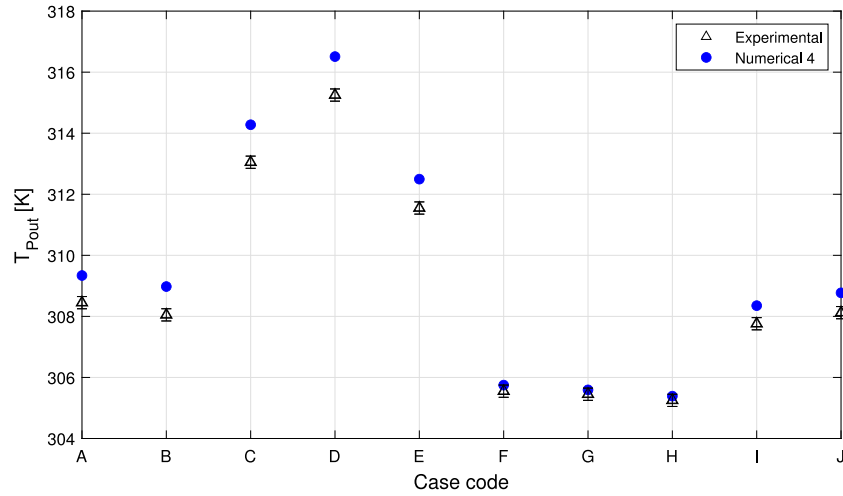**Fig. 9.** Secondary air outlet temperatures for all the validation cases.

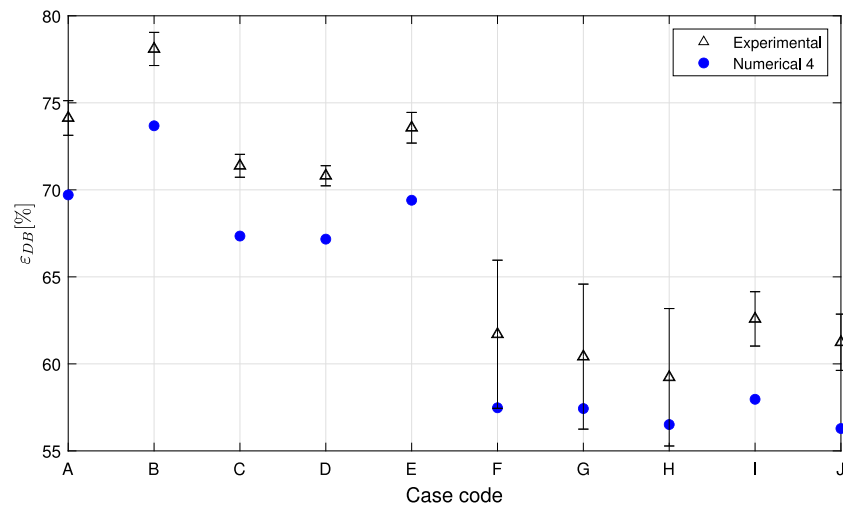**Fig. 10.** Primary air outlet temperatures for all the validation cases.

Fig. 11. Dry-bulb effectiveness for all the validation cases.
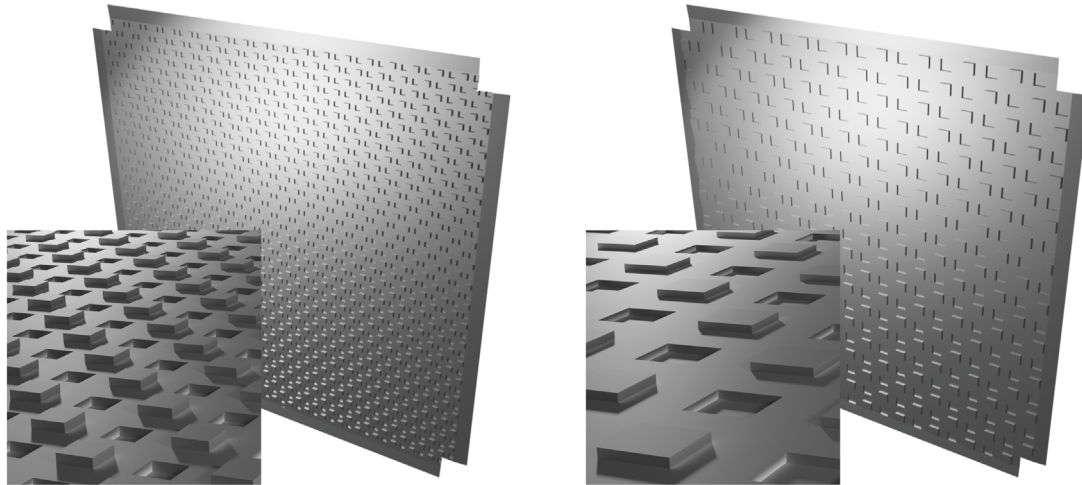
Fig. 12. Examples of two plates with dimples in the shape of parallelepipeds with squared section.

Table 5
Summary of the characteristics of the analyzed dimples.

Dimple code	Dimple type	Main dimension [mm]	Spacing [mm]
N	None	–	–
SC	Spherical caps	20	30
P-12-12	Parallelepipeds	12	12
P-9-9	Parallelepipeds	9	9
P-6-6	Parallelepipeds	6	6
P-9-3	Parallelepipeds	9	3

dimples in the shape of parallelepipeds with squared section, having different sizes and spacing between their extremities, were analyzed. A schematic representation of two examples of plates with these new dimples is shown in Fig. 12.

The manufacturability of the plates for the new analyzed geometries was not evaluated in this work, as it was preferred to first investigate the potential performance of such geometries in their ideal version. Moreover, this choice was also motivated by the fact that the innovative manufacturing techniques are rapidly changing what is realizable and affordable, so a different extensive study could be devoted to the investigation of the manufacturing aspect.

Table 5 summarizes all the dimples analyzed, describing their type, their main dimension (maximum diameter for dimples in the shape of spherical caps, length of the section side for dimples in the shape of parallelepipeds), and the spacing between the extremities of two adjacent dimples. The height is the same for all the cases and it is equal to 1.615 mm.

In addition to dry-bulb effectiveness, pressure losses along the channels must also be taken into account. In fact, if they increase excessively, it is necessary to provide a higher mechanical power upstream of the recuperator to ensure the desired flow velocity, thus increasing the energy consumption and reducing the advantage of a higher effectiveness. For this reason, it is necessary to look for a plate shape which is able to significantly enhance the performance, without an excessive increase in pressure drop along the channels.

Fig. 13 shows the results of dry-bulb effectiveness (in blue) and maximum pressure loss along the channels, ΔP_{MAX} (in red), for cases C and I with all the plates shapes analyzed.

As previously mentioned, the difference between the plate with real dimples in the shape of spherical caps and the flat plate with no dimples is not significant in terms of dry-bulb effectiveness. On the contrary, using dimples with squared section helps improving the thermal performance, as it constitutes a suitable obstacle to significantly alter the

fluid flow. In particular, the best effectiveness enhancement is obtained with "P-9-3" dimples, namely parallelepipeds with 9 mm section side and 3 mm spacing between their extremities. This plate shape allows to increase the dry-bulb effectiveness of 21.0–22.8% with respect to the plate with spherical caps. However, in this case, the maximum pressure loss along the channel is about 35 times that obtained in the case with "SC" dimples, so this solution is not practically applicable, as the pressure loss is too large. This behavior is probably due to the reduced spacing between the dimples, which leads to the formation of very narrow passages for the air flow, so that the local velocity increases, thus favoring the onset of turbulence and improving the heat exchange, but also increasing a lot the pressure losses.

A good trade-off between performance enhancement and restrained pressure loss increase is obtained with "P-6-6" dimples, namely parallelepipeds with 6 mm section side and 6 mm spacing between their extremities. In fact, in this case, the dry-bulb effectiveness increase is about 12.5–15.9% with respect to the case with "SC" dimples, and the maximum pressure loss is about 4–5 times the original one, so it can be considered still acceptable, especially in sectors for which a significant increase in thermal effectiveness is fundamental, while the worsening of pressure losses is not particularly significant.

The difference in the velocity and temperature fields between the case with "SC" dimples and the case with "P-6-6" dimples can be seen in Figs. 14–17.

In particular, Figs. 14 and 15 show the streamwise component of primary air velocity obtained in simulation C for four time steps in a statistically-steady condition, with "SC" and "P-6-6" dimples, respectively. From these figures, it is possible to notice that as "SC" dimples are very flat, smooth, and spaced, the maximum velocity reached in this case is much lower than the one obtained with "P-6-6" dimples, which form very narrow channels that lead to a significant increase in the air velocity. As a consequence, as previously mentioned, with this new geometry the heat exchange is facilitated by the turbulent vortices which cause mixing of the flow. However, the air passages are not too narrow as when using "P-9-3" dimples, so the pressure losses increase is still acceptable.

The effects of the velocity increase are also evident from the temperature fields. In particular, Figs. 16 and 17 show the primary air temperature obtained in simulation C for four time steps in a statistically-steady condition, with "SC" and "P-6-6" dimples, respectively. From these figures, it is possible to notice that the vortex streets obtained in the case with "SC" dimples are always unmixed, thus forming independent channels where the air can flow undisturbed. On the contrary,
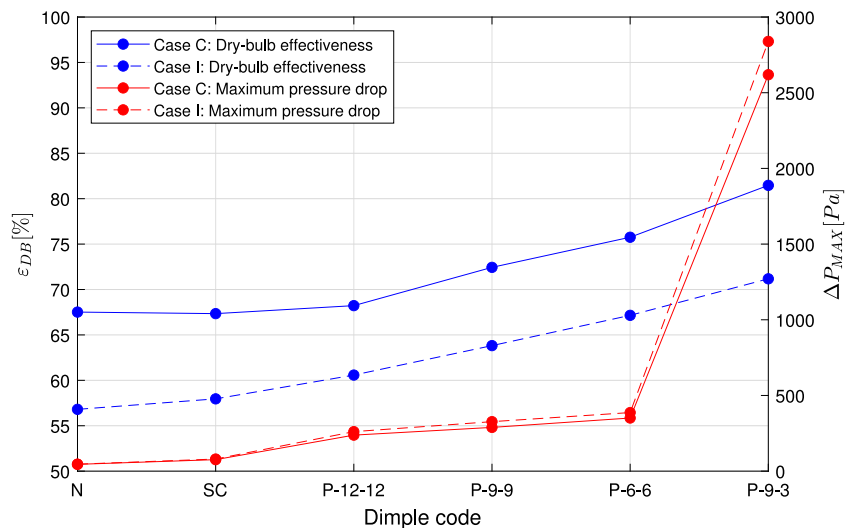
Fig. 13. Dry-bulb effectiveness and maximum pressure loss along the channels for cases C and I with all the plates shapes analyzed.
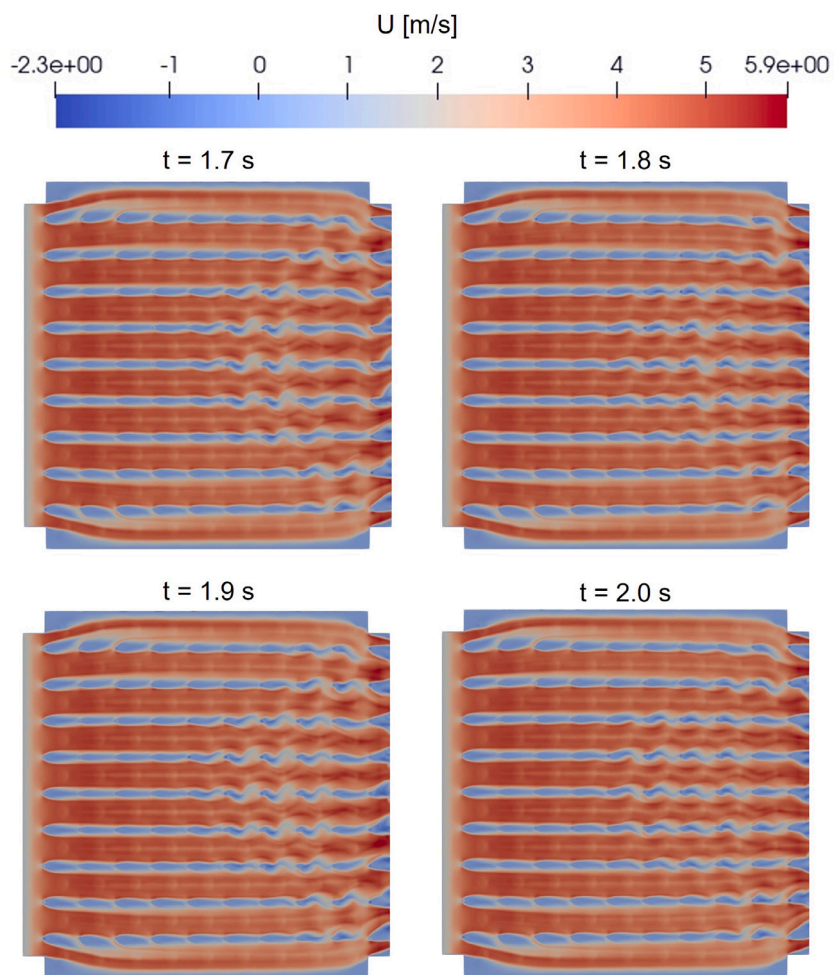

Fig. 14. Streamwise component of primary air velocity for time steps 1.7, 1.8, 1.9, and 2.0 s in the simulation of case C with "SC" dimples.
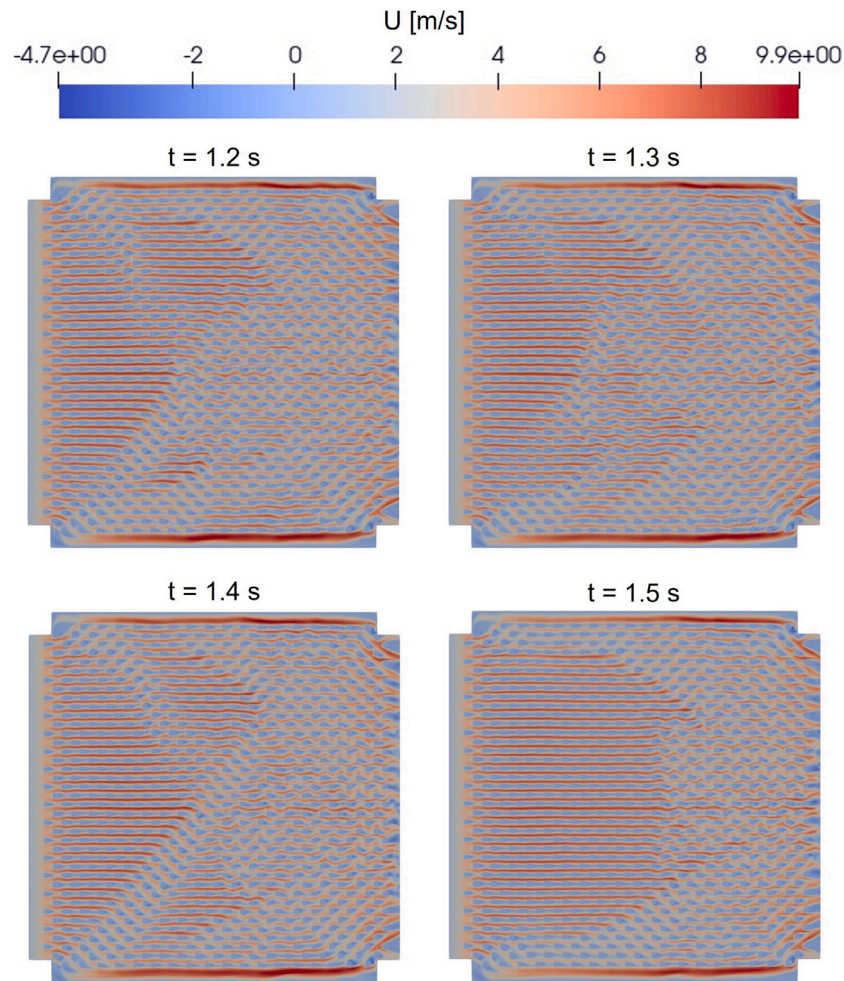
Fig. 15. Streamwise component of primary air velocity for time steps 1.2, 1.3, 1.4, and 1.5 s in the simulation of case C with "P-6-6" dimples.

when using "P-6-6" dimples, the channels that form are too narrow not to influence each other, so each vortex street is no more independent from the others, thus improving the heat exchange and resulting in a much lower primary air outlet temperature, namely a much higher effectiveness.

Therefore, from this study it emerges that, in the design of IEC recuperators, it is necessary to use plate geometries that allow to form channels narrow enough to create vortex streets dependent on each other, in order to induce the flow mixing, thus favoring the onset of turbulence and improving the heat transfer. However, it is necessary to take into account that if the channels are too narrow, the pressure drop will increase excessively, thus reducing the benefit obtainable with the improvement of the cooling performance. Therefore, it is important to find a good trade-off between a significant increase in dry-bulb effectiveness and the restraint of pressure losses along the channels.

Moreover, the obstacles encountered by the flow must not be too flat and smooth. In fact, if the ratio between the height and the base of the dimples is too low, the mixing, and thus the heat exchange, is not effective.

Finally, it is worth mentioning that the model developed in this work can be used in the early design of IEC recuperators, both to test different flow conditions, and to try new geometries able to improve the heat exchanger performance, thus reducing the need of long and expensive experimental campaigns. However, this model can be employed only if the evaporative process occurs before the secondary air enters the recuperator. Therefore, further studies are needed to extend the possibility of using the model also to recuperators with wet secondary channels.

6. Conclusions

In this study, a CFD model for design and performance prediction of recuperators for IEC systems with dry primary and secondary channels was developed and validated against experimental results. Then, the model was used to find a new plate geometry which guarantees performance enhancement with restrained pressure losses along the channels.

The main findings of this analysis can be summarized as follows:

- In transient conditions, with second order discretization schemes, and turbulent ($k - \omega \, SST$) settings, the average and maximum difference between numerical and experimental results are 1.7% and 4.9% for the secondary air outlet temperature, 4.0% and 5.3% for the primary air outlet temperature, and 6.0% and 8.1% for the dry-bulb effectiveness, respectively.
- Using a commercial dimpled aluminum plate, with dimples in the shape of spherical caps, having a base diameter of 20 mm, a height of 1.615 mm, and a spacing between their extremities of 30 mm, does not practically increase the heat transfer along the plate with respect to using a flat plate without dimples. In fact, these dimples are only useful to guarantee mechanical stiffness, but they are too flat and smooth to induce the flow mixing.
- Among the configurations analyzed in this study, the maximum heat transfer performance enhancement is obtained using a plate with dimples in the shape of parallelepipeds with squared section, having a square side of 9 mm and a spacing of 3 mm between
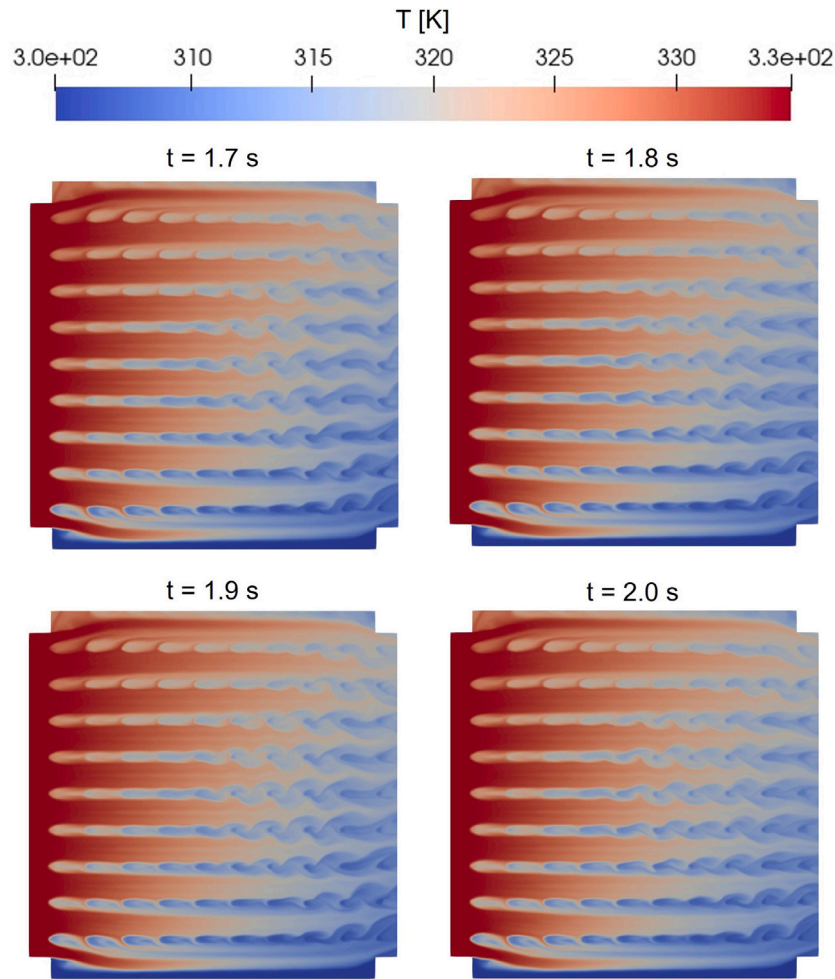
Fig. 16. Primary air temperature for time steps 1.7, 1.8, 1.9, and 2.0 s in the simulation of case C with "SC" dimples.

their extremities. However, despite a 21–23% increase in dry-bulb effectiveness, the maximum pressure loss along the channels is approximately 35 times higher than that obtained with the original dimples, so this solution is not acceptable.

- A good trade-off between increasing dry-bulb effectiveness (+13–16%) and maintaining restrained pressure losses (4–5 times the original ones) was obtained with dimples in the shape of parallelepipeds with squared section, having a square side of 6 mm and a spacing of 6 mm between their extremities.
- In the design of recuperators for IEC systems, it is beneficial to use plates geometries that form channels narrow enough to create vortex streets dependent on each other, to induce the flow mixing and improve the cooling performance. However, the channels should not be too narrow, as this could increase the pressure losses in the recuperator, thus reducing the benefit due to the effectiveness improvement.
- The model developed in this work can be used for the early design and optimization of IEC heat exchangers with dry secondary channels, reducing the necessity of extensive experimental campaigns.

CRediT authorship contribution statement

Roberta Caruana: Writing – review & editing, Writing – original draft, Visualization, Validation, Methodology, Investigation, Formal analysis, Conceptualization. **Luca Marocco:** Writing – review & editing, Software, Methodology, Investigation, Conceptualization. **Manfredo**

Guilizzoni: Writing – review & editing, Supervision, Methodology, Investigation, Formal analysis, Conceptualization.

Declaration of competing interest

The authors declare that they have no known competing financial interests or personal relationships that could have appeared to influence the work reported in this paper.

Data availability

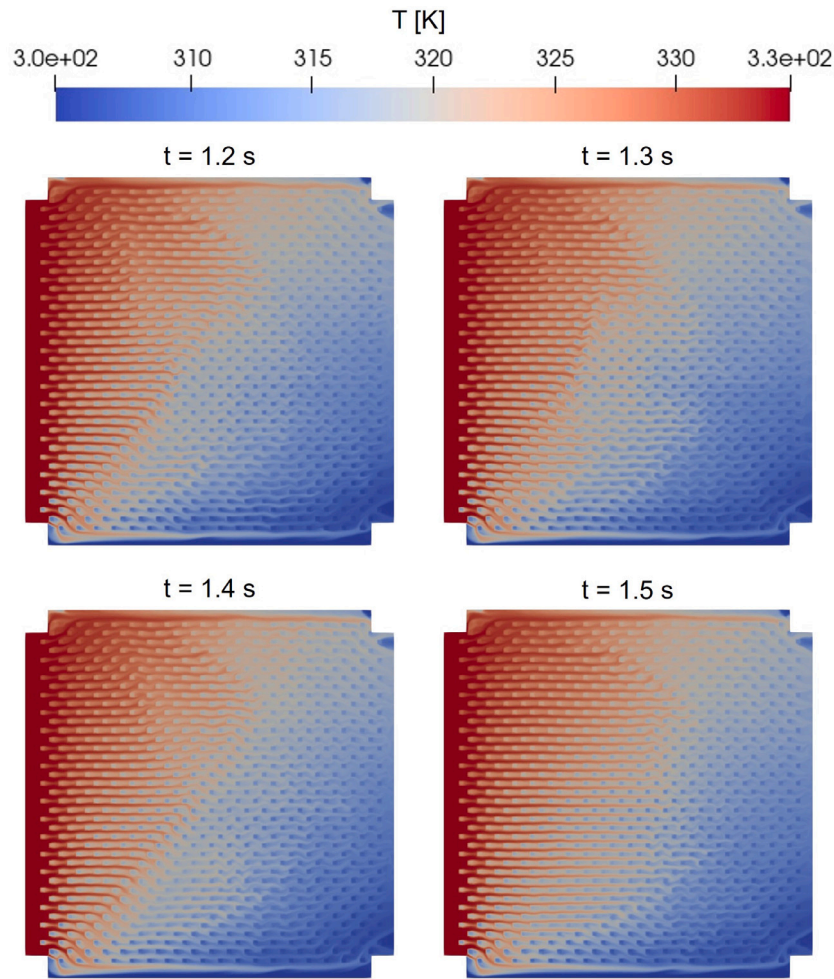Data will be made available on request.

Fig. 17. Primary air temperature for time steps 1.2, 1.3, 1.4, and 1.5 s in the simulation of case C with "P-6-6" dimples.

References

[1] U. Sajjad, N. Abbas, K. Hamid, S. Abbas, I. Hussain, S.M. Ammar, M. Sultan, H.M. Ali, M. Hussain, C.C. Wang, et al., A review of recent advances in indirect evaporative cooling technology, Int. Commun. Heat Mass Transfer 122 (2021) 105–140, http://dx.doi.org/10.1016/j.icheatmasstransfer.2021.105140.

[2] A. Ghosh, J. Bhattacharya, A solar regenerated liquid desiccant evaporative cooling system for office building application in hot and humid climate, Therm. Sci. Eng. Prog. 22 (2021) 100804, http://dx.doi.org/10.1016/j.tsep.2020.100804.

[3] R. Caruana, S. De Antonellis, L. Marocco, P. Liberati, M. Guilizzoni, Experimental characterization of the wettability of coated and uncoated plates for indirect evaporative cooling systems, Fluids 8 (4) (2023) 122, http://dx.doi.org/10.3390/fluids8040122.

[4] R. Caruana, L. Marocco, P. Liberati, M. Guilizzoni, Experimental analysis of the effect of limescale on the wettability of indirect evaporative cooling system plates, Fluids 9 (3) (2024) 76, http://dx.doi.org/10.3390/fluids9030076.

[5] A. Pacak, W. Worek, Review of dew point evaporative cooling technology for air conditioning applications, Appl. Sci. 11 (3) (2021) 934, http://dx.doi.org/10.3390/app11030934.

[6] M.A. Jamil, N. Imtiaz, K.C. Ng, B.B. Xu, H. Yaqoob, M. Sultan, M.W. Shahzad, Experimental and parametric sensitivity analysis of a novel indirect evaporative cooler for greener cooling, Therm. Sci. Eng. Prog. 42 (2023) 101887, http://dx.doi.org/10.1016/j.tsep.2023.101887.

[7] S. Moshari, G. Heidarinejad, A. Fathipour, Numerical investigation of wet-bulb effectiveness and water consumption in one-and two-stage indirect evaporative coolers, Energy Convers. Manage. 108 (2016) 309–321, http://dx.doi.org/10.1016/j.enconman.2015.11.022.

[8] Z. Duan, C. Zhan, X. Zhang, M. Mustafa, X. Zhao, B. Alimohammadisagvand, A. Hasan, Indirect evaporative cooling: Past, present and future potentials, Renew. Sustain. Energy Rev. 16 (9) (2012) 6823–6850, http://dx.doi.org/10.1016/j.rser.2012.07.007.

[9] B. Porumb, P. Ungureşan, L.F. Tutunaru, A. Şerban, M. Bălan, A review of indirect evaporative cooling technology, Energy Procedia 85 (2016) 461–471, http://dx.doi.org/10.1016/j.egypro.2015.12.228.

[10] H. Yang, W. Shi, Y. Chen, Y. Min, Research development of indirect evaporative cooling technology: An updated review, Renew. Sustain. Energy Rev. 145 (2021) 111082, http://dx.doi.org/10.1016/j.rser.2021.111082.

[11] P.M. Cuce, S. Riffat, A state of the art review of evaporative cooling systems for building applications, Renew. Sustain. Energy Rev. 54 (2016) 1240–1249, http://dx.doi.org/10.1016/j.rser.2015.10.066.

[12] I.M.A. Aljubury, H.D. Ridha, Enhancement of evaporative cooling system in a greenhouse using geothermal energy, Renew. Energy 111 (2017) 321–331, http://dx.doi.org/10.1016/j.renene.2017.03.080.

[13] C.J. Testa, K. Shvedova, C. Hu, W. Wu, S.C. Born, B. Takizawa, S. Mascia, Heterogeneous crystallization as a process intensification technology in an integrated continuous manufacturing process for pharmaceuticals, Org. Process Res. Dev. 25 (2) (2021) 225–238, http://dx.doi.org/10.1021/acs.oprd.0c00468.

[14] R. Caruana, S. De Antonellis, L. Marocco, M. Guilizzoni, Modeling of indirect evaporative cooling systems: A review, Fluids 8 (11) (2023) 303, http://dx.doi.org/10.3390/fluids8110303.

[15] J.S.J. Alonso, F.R. Martinez, E.V. Gomez, M.A.-G. Plasencia, Simulation model of an indirect evaporative cooler, Energy Build. 29 (1) (1998) 23–27, http://dx.doi.org/10.1016/S0378-7788(98)00014-0.

[16] N. Stoitchkov, G. Dimitrov, Effectiveness of crossflow plate heat exchanger for indirect evaporative cooling: Efficacité des échangeurs thermiques à plaques, à courants croises pour refroidissement indirect évaporatif, Int. J. Refrig. 21 (6) (1998) 463–471, http://dx.doi.org/10.1016/S0140-7007(98)00004-8.

[17] C. Ren, H. Yang, An analytical model for the heat and mass transfer processes in indirect evaporative cooling with parallel/counter flow configurations, Int. J. Heat Mass Transfer 49 (3–4) (2006) 617–627, http://dx.doi.org/10.1016/j.ijheatmasstransfer.2005.08.019.

[18] A. Hasan, Going below the wet-bulb temperature by indirect evaporative cooling: analysis using a modified ε-NTU method, Appl. Energy 89 (1) (2012) 237–245, http://dx.doi.org/10.1016/j.apenergy.2011.07.005.

[19] Z. Liu, W. Allen, M. Modera, Simplified thermal modeling of indirect evaporative heat exchangers, HVAC&R Res. 19 (3) (2013) 257–267, http://dx.doi.org/10.1080/10789669.2013.763653.

[20] X. Cui, K. Chua, M. Islam, W. Yang, Fundamental formulation of a modified LMTD method to study indirect evaporative heat exchangers, Energy Convers. Manage. 88 (2014) 372–381, http://dx.doi.org/10.1016/j.enconman.2014.08.056.

[21] Y. Chen, Y. Luo, H. Yang, A simplified analytical model for indirect evaporative cooling considering condensation from fresh air: Development and application, Energy Build. 108 (2015) 387–400, http://dx.doi.org/10.1016/j.enbuild.2015.09.054.

[22] S. De Antonellis, C.M. Joppolo, P. Liberati, S. Milani, F. Romano, Modeling and experimental study of an indirect evaporative cooler, Energy Build. 142 (2017) 147–157, http://dx.doi.org/10.1016/j.enbuild.2017.02.057.

[23] P. Liberati, S. De Antonellis, C. Leone, C.M. Joppolo, Y. Bawa, Indirect Evaporative cooling systems: Modelling and performance analysis, Energy Procedia 140 (2017) 475–485, http://dx.doi.org/10.1016/j.egypro.2017.11.159.

[24] F. Comino, S. Milani, S. De Antonellis, C.M. Joppolo, M.R. de Adana, Simplified performance correlation of an indirect evaporative cooling system: Development and validation, Int. J. Refrig. 88 (2018) 307–317, http://dx.doi.org/10.1016/j.ijrefrig.2018.02.002.

[25] B. Zheng, C. Guo, T. Chen, Q. Shi, J. Lv, Y. You, Development of an experimental validated model of cross-flow indirect evaporative cooler with condensation, Appl. Energy 252 (2019) 113438, http://dx.doi.org/10.1016/j.apenergy.2019.113438.

[26] X. Zhao, J. Li, S. Riffat, Numerical study of a novel counter-flow heat and mass exchanger for dew point evaporative cooling, Appl. Therm. Eng. 28 (14–15) (2008) 1942–1951, http://dx.doi.org/10.1016/j.applthermaleng.2007.12.006.

[27] B. Riangvilaikul, S. Kumar, Numerical study of a novel dew point evaporative cooling system, Energy Build. 42 (11) (2010) 2241–2250, http://dx.doi.org/10.1016/j.enbuild.2010.07.020.

[28] X. Cui, K. Chua, W. Yang, Numerical simulation of a novel energy-efficient dew-point evaporative air cooler, Appl. Energy 136 (2014) 979–988, http://dx.doi.org/10.1016/j.apenergy.2014.04.040.

[29] Y. Wan, C. Ren, L. Xing, An approach to the analysis of heat and mass transfer characteristics in indirect evaporative cooling with counter flow configurations, Int. J. Heat Mass Transfer 108 (2017) 1750–1763, http://dx.doi.org/10.1016/j.ijheatmasstransfer.2017.01.019.

[30] Y. Wan, J. Lin, K.J. Chua, C. Ren, A new method for prediction and analysis of heat and mass transfer in the counter-flow dew point evaporative cooler under diverse climatic, operating and geometric conditions, Int. J. Heat Mass Transfer 127 (2018) 1147–1160, http://dx.doi.org/10.1016/j.ijheatmasstransfer.2018.07.142.

[31] Y. Wan, J. Lin, K.J. Chua, C. Ren, Similarity analysis and comparative study on the performance of counter-flow dew point evaporative coolers with experimental validation, Energy Convers. Manage. 169 (2018) 97–110, http://dx.doi.org/10.1016/j.enconman.2018.05.043.

[32] J. Lin, D.T. Bui, R. Wang, K.J. Chua, On the fundamental heat and mass transfer analysis of the counter-flow dew point evaporative cooler, Appl. Energy 217 (2018) 126–142, http://dx.doi.org/10.1016/j.apenergy.2018.02.120.

[33] Y. You, H. Jiang, J. Lv, Analysis of influence of IEC heat exchanger based on CFD method, Energy Procedia 158 (2019) 5759–5764, http://dx.doi.org/10.1016/j.egypro.2019.01.555.

[34] Y. Min, Y. Chen, H. Yang, Numerical study on indirect evaporative coolers considering condensation: A thorough comparison between cross flow and counter flow, Int. J. Heat Mass Transfer 131 (2019) 472–486, http://dx.doi.org/10.1016/j.ijheatmasstransfer.2018.11.082.

[35] A. Pakari, S. Ghani, Regression models for performance prediction of counter flow dew point evaporative cooling systems, Energy Convers. Manage. 185 (2019) 562–573, http://dx.doi.org/10.1016/j.enconman.2019.02.025.

[36] A. Pakari, S. Ghani, Comparison of 1D and 3D heat and mass transfer models of a counter flow dew point evaporative cooling system: Numerical and experimental study, Int. J. Refrig. 99 (2019) 114–125, http://dx.doi.org/10.1016/j.ijrefrig.2019.01.013.

[37] Y. Liu, J.M. Li, X. Yang, X. Zhao, Two-dimensional numerical study of a heat and mass exchanger for a dew-point evaporative cooler, Energy 168 (2019) 975–988, http://dx.doi.org/10.1016/j.energy.2018.11.135.

[38] C. Guo, Q. Liu, B. Zheng, Y. You, Y. Li, Development of model based on condensation area ratio and effect on heat transfer capacity of indirect evaporative cooling, Appl. Therm. Eng. 164 (2020) 114557, http://dx.doi.org/10.1016/j.applthermaleng.2019.114557.

[39] Y. Wan, A. Soh, Y. Shao, X. Cui, Y. Tang, K.J. Chua, Numerical study and correlations for heat and mass transfer coefficients in indirect evaporative coolers with condensation based on orthogonal test and CFD approach, Int. J. Heat Mass Transfer 153 (2020) 119580, http://dx.doi.org/10.1016/j.ijheatmasstransfer.2020.119580.

[40] A. Adam, D. Han, W. He, J. Chen, Numerical analysis of cross-flow plate type indirect evaporative cooler: Modeling and parametric analysis, Appl. Therm. Eng. 185 (2021) 116379, http://dx.doi.org/10.1016/j.applthermaleng.2020.116379.

[41] W. Shi, Y. Min, Y. Chen, H. Yang, Development of a three-dimensional numerical model of indirect evaporative cooler incorporating with air dehumidification, Int. J. Heat Mass Transfer 185 (2022) 122316, http://dx.doi.org/10.1016/j.ijheatmasstransfer.2021.122316.

[42] F. Comino, M.J. Romero-Lara, M.R. de Adana, Experimental and numerical study of dew-point indirect evaporative coolers to optimize performance and design, Int. J. Refrig. 142 (2022) 92–102, http://dx.doi.org/10.1016/j.ijrefrig.2022.06.006.

[43] A. Adam, D. Han, W. He, M. Amidpour, H. Zhong, Numerical investigation of the heat and mass transfer process within a cross-flow indirect evaporative cooling system for hot and humid climates, J. Build. Eng. 45 (2022) 103499, http://dx.doi.org/10.1016/j.jobe.2021.103499.

[44] G. Zhu, W. Chen, D. Zhang, T. Wen, Performance evaluation of counter flow dew-point evaporative cooler with a three-dimensional numerical model, Appl. Therm. Eng. 219 (2023) 119483, http://dx.doi.org/10.1016/j.applthermaleng.2022.119483.

[45] A. Pacak, B. Baran, K. Sierpowski, Z. Malecha, D. Pandelidis, Application of computational fluid dynamics (CFD) methods to analyze energy efficiency of indirect evaporative coolers, Int. Commun. Heat Mass Transfer 143 (2023) 106727, http://dx.doi.org/10.1016/j.icheatmasstransfer.2023.106727.

[46] A. Adam, D. Han, W. He, Q. Shi, J. Chen, H. Zhong, The influences of the plate shape on the performance of the indirect evaporative cooler based on the CFD approach, J. Braz. Soc. Mech. Sci. Eng. 45 (2) (2023) 123, http://dx.doi.org/10.1007/s40430-023-04044-w.

[47] X. Ma, W. Shi, H. Yang, Improving the performance of indirect evaporative cooler for energy recovery from the perspective of nozzle configuration: A CFD model analysis, J. Build. Eng. (2023) 107195, http://dx.doi.org/10.1016/j.jobe.2023.107195.

[48] S. De Antonellis, M. Intini, C.M. Joppolo, Desiccant wheels effectiveness parameters: correlations based on experimental data, Energy Build. 103 (2015) 296–306, http://dx.doi.org/10.1016/j.enbuild.2015.06.041.

[49] S. De Antonellis, M. Intini, C.M. Joppolo, L. Molinaroli, F. Romano, Desiccant wheels for air humidification: An experimental and numerical analysis, Energy Convers. Manage. 106 (2015) 355–364, http://dx.doi.org/10.1016/j.enconman.2015.09.034.

[50] S. De Antonellis, C.M. Joppolo, P. Liberati, S. Milani, L. Molinaroli, Experimental analysis of a cross flow indirect evaporative cooling system, Energy Build. 121 (2016) 130–138, http://dx.doi.org/10.1016/j.enbuild.2016.03.076.

[51] Guide 98-3: Uncertainty of Measurement, Part 3: Guide to the Expression of Uncertainty in Measurement, International Organization for Standardization/International Electrotechnical Commission, 2008.

[52] F.R. Menter, Improved Two-Equation K-Omega Turbulence Models for Aerodynamic Flows, Tech. rep., 1992.